Monte Carlo model of electron transport for the calculation of Mars dayglow emissions

V. I. Shematovich, D. V. Bisikalo, J.-C. Gérard, Christopher M. Cox, S. W. Bougher, François Leblanc

Monte Carlo model of electron transport for the calculation of Mars dayglow emissions

V. I. Shematovich,[1] D. V. Bisikalo,[1] J.-C. Gérard,[2] C. Cox,[2] S. W. Bougher,[3] and F. Leblanc[4]

Received 9 May 2007; revised 7 December 2007; accepted 27 December 2007; published 26 February 2008.

[1] A model of the photoelectron collision-induced component of the Mars dayglow using recent cross sections and solar flux is described. The calculation of the photoelectron source of excitation is based on a stochastic solution of the Boltzmann equation using the direct simulation Monte Carlo method. The neutral atmosphere is taken from outputs of a global circulation model, and recent inelastic collision cross sections are adopted. The calculated vertical profiles of the CO Cameron bands and CO_2^+ doublet emissions integrated along the line of sight compare well with the Spectroscopy for the Investigation of the Characteristics of the Atmosphere of Mars (SPICAM) limb profiles observed with the SPICAM spectrograph on board Mars Express made at Ls = 166° during the summer season at northern midlatitudes. The comparison shows agreement to within the uncertainties of the excitation cross sections. Seasonal changes in the brightness and the altitude of the emission peaks are predicted with intensity variations in the range 15–20%.

Citation: Shematovich, V. I., D. V. Bisikalo, J.-C. Gérard, C. Cox, S. W. Bougher, and F. Leblanc (2008), Monte Carlo model of electron transport for the calculation of Mars dayglow emissions, *J. Geophys. Res.*, *113*, E02011, doi:10.1029/2007JE002938.

1. Introduction

[2] Since 1969, four space missions to Mars have carried a UV detector on board: the Mariner 6, 7, and 9 spacecraft [*Barth et al.*, 1971, 1972; *Stewart et al.*, 1972] with UV spectrometers and the Mars Express mission (MEX) with the Spectroscopy for the Investigation of the Characteristics of the Atmosphere of Mars (SPICAM) spectrograph [*Bertaux et al.*, 2000, 2006]. The best quality UV spectra of Mars were measured by the Hopkins Ultraviolet Telescope [*Feldman et al.*, 2000] and Far Ultraviolet Spectroscopic Explorer [*Krasnopolsky and Feldman*, 2002] Earth-orbiting observatories. However, these spectra were not spatially resolved. The main emission features of the Martian UV dayglow were observed for the first time by the Mariner 6, 7, and 9 UV spectrometers in the wavelength range 110–400 nm [*Barth et al.*, 1971, 1972]. *Barth et al.* [1971] analyzed the Mariner data and showed that these dayglow features are mainly produced by photon and photoelectron excitation of CO_2 between 100 and 200 km in altitude.

[3] Recent airglow measurements with the SPICAM spectrograph confirm the previous observations. According to *Leblanc et al.* [2006] the Mariner 9 spectrometer and SPICAM display the same features within the spectral range 110–305 nm, mainly the H Lyman-α emission at 121.6 nm, the atomic O multiplets at 130.4 nm and 135.6 nm, the CO fourth positive ($A^1\Pi - X^1\Sigma^+$) band system, several carbon emission lines between 140 and 170 nm, the CO Cameron band system ($a^3\Pi - X^1\Sigma^+$) between 190 and 270 nm, the CO_2^+ ultraviolet doublet ($B^2\Sigma^+ - X^2\Pi$) emission near 289 nm, and the O ($^1S - ^3P$) emission line at 297.2 nm. The relative brightness distribution of the different vibrational states within the Cameron band system observed by SPICAM is in a good agreement with the Mariner 9 observations as well as the relative intensities of the CO_2^+ ($B^2\Sigma^+ - X^2\Pi$) emission at 289 nm and of the total Cameron band system emission [*Leblanc et al.*, 2006].

[4] Theoretical analyses of the different emissions of the Martian ultraviolet dayglow for the conditions of the Viking 1 measurements were made by *Mantas and Hanson* [1979] and *Fox and Dalgarno* [1979]. Since then some of the main inputs used to model the airglow emissions such as the solar flux representation and the excitation cross sections have been reestimated. To quantitatively analyze the SPICAM spectra now available, it is useful to rely on an updated model of electron transport in the Martian thermosphere since electron impact is among the key processes leading to excitation of these emissions. Therefore we have developed a model describing electron transport in the Martian atmosphere using a Monte Carlo algorithm. This model will be applied to the analysis of some of the ultraviolet emissions observed with SPICAM.

2. Model of Electron Transport and Thermalization

[5] We first describe the numerical model used to calculate the photoelectron production and energy degradation in

[1]Institute of Astronomy, Russian Academy of Sciences, Moscow, Russia.
[2]Laboratoire de Physique Atmosphérique et Planétaire, Université de Liège, Liege, Belgium.
[3]Atmospheric, Oceanic and Space Sciences, College of Engineering, University of Michigan, Ann Arbor, Michigan, USA.
[4]Service d'Aéronomie du CNRS, Verrières-le-Buisson, France.

0148-0227/08/2007JE002938

the Martian atmosphere. Electron transport is usually treated by models that can be broadly divided into three categories: continuous loss models, two-stream or multistream models, and Monte Carlo models. The models from the latter category require a sophisticated level of numerical complexity and are time-consuming; however, they integrate physical processes in a direct way, and at some level they are the most realistic simulations [*Solomon*, 2001].

2.1. Photochemical Processes

[6] In the daytime thermosphere of Mars, energetic electrons are produced by photoionization of the main atmospheric constituents by EUV and X-ray solar radiations. These newly formed electrons are transported in the thermosphere where they lose their kinetic energy in elastic, inelastic, and ionization collisions with the ambient atmospheric gas:

$$e(E) + X \rightarrow \begin{cases} e(E') + X \\ e(E') + X^* \\ e(E') + X^+ + e(E_s), \end{cases}$$

where E and $E'(<E)$ are the kinetic energies of the primary electron before and after a collision; $X = CO_2$, CO, O, or N_2; X^* and X^+ are atmospheric species in excited and ionized states, respectively; and E_s is the energy of the secondary electron formed in the ionizing collision. We consider the following neutral and ionized excited states for the main atmospheric species: (1) excitation and dissociative excitation of $CO_2^* = CO_2$ ($v(010)$, $v(100)$, $v(001)$, electronic states at 8.6, 9.3, 11.1, 12.4, and 13.6 eV [see, e.g., *Sawada et al.*, 1972a]; (2) direct ionization of $CO_2 \rightarrow CO_2^+(X\,^2\Pi, A\,^2\Pi, B\,^2\Sigma, C\,^2\Sigma)$; (3) dissociative ionization of $CO_2 \rightarrow CO^+ + O$, $O^+ + CO$, $C^+ + O_2$; (4) excitation of $CO^* = CO(a\,^3\Pi, A\,^1\Pi$, electronic state at 13.5 eV [see, e.g., *Sawada et al.*, 1972b]; (5) direct ionization of $CO \rightarrow CO^+(X\,^2\Sigma, A\,^2\Pi, B\,^2\Sigma)$; (6) dissociative ionization of $CO \rightarrow C^+ + O$, $O^+ + C$; (7) excitation of $O^* = O(^1D - 1.96$ eV, $^1S - 4.17$eV, $3s^5S^0 - 9.29$ eV, $3s\,^3S^0 - 9.53$ eV, $3p^5P^0 - 10.76$ eV, $3p\,^3P^0 - 10.97$ eV, $3d^3D^0 - 12.07$ eV, $3s\,^3{}'D^0 - 12.54$ eV); (8) direct ionization of $O \rightarrow O^+$ (^4S, ^2D, ^2P); (9) direct ionization of $N_2 \rightarrow N_2^+$; (10) excitation and dissociative excitation of N_2^*; and (11) dissociative ionization of $N_2 \rightarrow N^+ + N$.

[7] If the collision produces ionization, a secondary electron is created, and an isotropically distributed pitch angle is randomly assigned as well as an energy, using an integral form of the approximate formula of *Green and Sawada* [1972] and *Jackman et al.* [1977] based on the laboratory results of *Opal et al.* [1971]:

$$\int_0^{E_s} \sigma_{i,j}(E_p, E_l')dE_l' = A(E_p)\Gamma(E_p)\left[\tan^{-1}\left(\frac{E_s - T_0(E_p)}{\Gamma(E_p)}\right) + c\right],$$

where $\sigma_{i,j}$ is the state-specific cross section for species i and state j at primary electron energy E_p and secondary electron energy E_s, $A(E_p)$, $\Gamma(E_p)$, and $T_0(E_p)$ are fitting functions defined by the tabulated parameters of *Jackman et al.* [1977], and $c = \tan^{-1}[T_0(E_p)/\Gamma(E_p)]$. By equating the integral to a random number r, dropping the leading constants, and solving for E_s, randomized secondary electron generation functions distributed according to the above parameterizations are obtained:

$$E_s = \Gamma(E_p)\tan(r - c) + T_0(E_p),$$

where r has been normalized over the interval 0 to $r_{\max}$:

$$r_{\max} = \tan^{-1}\left(\frac{E_{s_{\max}} - T_0(E)}{\Gamma(E)}\right) + c; \quad E_{s_{\max}} = \frac{E_p - E_{\text{ion}}}{2}.$$

If the collision is elastic, a new pitch angle is randomly assigned to the electron using expressions and parameters developed by *Porter and Jump* [1978] and *Porter et al.* [1987] for angular scattering of electrons. This phenomenological extension to the screened Rutherford formula allows a backscattering lobe at low energy:

$$\sigma(\theta) = \alpha\left(\frac{1}{(1 + 2\gamma - \cos\theta)} + \frac{\beta}{(1 + 2\delta + \cos\theta)}\right),$$

where α, β, γ, and δ are fit parameters, tabulated as functions of energy by *Porter et al.* [1987]. The energy loss of photoelectrons and secondary electrons is dominated at low energies by elastic collisions with the ambient electrons.

[8] For inelastic collisions we use the forward scattering approximation: it is assumed that the differential cross section for these collisions is so strongly peaked in the forward direction that angular redistribution by this process is negligible. This is a good approximation at all but the lowest energies. Below 100 eV, there can be considerable backscatter, particularly from forbidden excitation transitions, but the flux becomes so isotropic and the relative size of the elastic cross sections becomes so large that this has little effect on the final pitch angle distribution [*Porter and Jump*, 1978].

2.2. Kinetic Equation

[9] The photoelectrons and precipitating electrons lose their excess kinetic energy in collisions with the ambient atmospheric particles. Their kinetics and transport is described by the kinetic Boltzmann equation:

$$\mathbf{v}\frac{\partial}{\partial \mathbf{r}}f_e + \mathbf{s}\frac{\partial}{\partial \mathbf{v}}f_e = Q_{e,\text{photo}}(\mathbf{v}) + Q_{e,\text{secondary}}(\mathbf{v}) + \sum_{M = \text{O,CO,N}_2\text{,CO}_2} J(f_e, f_M), \quad (1)$$

where $f_e(\mathbf{r},\mathbf{v})$, and $f_M(\mathbf{r},\mathbf{v})$ are the velocity distribution functions for electrons and for the species of the ambient gas, respectively. The left side of the kinetic equation describes the transport of electrons in the planetary gravitational field $\mathbf{s}$. In the right-hand side of the kinetic equation the $Q_{e,\text{photo}}$ term describes the formation rate of primary electrons due to photoionization, while the $Q_{e,\text{secondary}}$ term describes the rate of formation of the secondary electrons. The elastic and inelastic scattering terms J for electron collisions with ambient atmospheric

species are written in a standard form. It is assumed that the ambient atmospheric gas is characterized by the local Maxwellian velocity distribution functions.

2.3. Numerical Model

[10] The direct simulation Monte Carlo (DSMC) method is an efficient tool to solve kinetic equations for atmospheric systems in the stochastic approximation [*Shematovich et al.*, 1994; *Bisikalo et al.*, 1995; *Gérard et al.*, 2000]. The details of the numerical model have been described earlier [*Shematovich et al.*, 1994; *Bisikalo et al.*, 1995]. In the numerical simulations the evolution of the system of modeling particles due to collisional processes and particle transport is calculated from the initial to the steady state. In order to minimize boundary effects the lower boundary was set at an altitude of 75 km, and the upper boundary was fixed at 250 km, above which the computed excitation rates are small because of decreasing of neutral densities. The relative importance of the collisional processes is governed by their cross sections. The adopted cross sections are described in Section 3.2.

3. Model Input Parameters

3.1. Photoionization and Photoelectron Production Rates

[11] Solar extreme ultraviolet radiation photoionizes the neutral constituents of the upper atmosphere of Mars and produces fresh photoelectrons and ions. The energy of the ionizing photons generally exceeds the energy required for ionization, and the excess energy mainly goes into electron kinetic energy and into ion excitation energy. The initial photoelectron energy depends not only on the energy of the ionizing photon and the ionization potential of the neutral gas but also on the excitation state of the newly created ion. The expression used for the photoelectron production rate $P_e(E,z)$ is

$$P_e(E,z) = \sum_k \sum_l n_k(z) \int_0^{\lambda_k} d\lambda I_\infty(\lambda) \exp[-\tau(\lambda,z)] \sigma_k^i p_k(\lambda, E_l), \quad (2)$$

where the optical depth τ is

$$\tau(\lambda,z) = \sum_k \sigma_k^a(\lambda) \int_z^\infty n_k(z')dz',$$

n_k is the number density of the kth neutral constituent, and $\sigma_k^i(\lambda)$ and $\sigma_k^a(\lambda)$ are the wavelength-dependent total ionization and absorption cross sections, respectively. In equation (2), $p_k(\lambda, E_l)$ is the branching ratio for the excited ion state with an ionization threshold of E_l; the photoelectron energy is equal to $E = E_\lambda - E_l$, where E_λ is the energy corresponding to wavelength λ and λ_k is the ionization threshold wavelength for the kth neutral constituent. Finally, $I_\infty(\lambda)$ is the solar radiation flux at wavelength λ outside the atmosphere. We use the SOLAR2000 research grade v2.27 EUV solar spectrum model which provides fluxes in 39 wavelength bins and emission lines between 1.86 and 105.0 nm wavelengths [*Tobiska*, 2004].

3.2. Cross Sections

[12] The photoionization and absorption cross section data and branching ratios for CO_2, CO, O, and N_2 are taken from *Huebner et al.* [1992]. The electron impact cross sections for excitations of vibrational levels and for electronic states of CO_2 are given by *Itikawa* [2002] and *Sawada et al.* [1972a], respectively. For dissociative excitation of Cameron bands the semiempirical representation by *Sawada et al.* [1972a] scaled to the measurements by *Ajello* [1971] is routinely used. The upper state CO ($a^3\Pi$) of the Cameron band emissions is metastable with the relatively long radiative lifetime and is excited both directly by electron impact and indirectly by cascade. Furthermore, being a dissociative fragment of CO_2, CO ($a^3\Pi$) molecules are formed with an excess kinetic energy, and such excited molecules can escape from the excitation region. Accordingly, the emission of the Cameron system is blended with other emissions unless the excitation energy is small [*Furlong and Newell*, 1996]. Following discussions by *Itikawa* [2002] and *Furlong and Newell* [1996], we rescaled the Cameron system emission cross section to the peak value of 2.4×10^{-16} cm^2 at 80 eV based on the measurements by *Erdman and Zipf* [1983]. Because of the above mentioned difficulty of measurements the peak value is likely to have a large uncertainty of more than a factor of 2. Therefore when comparing the model calculations with SPICAM observations, it is necessary to keep in mind this significant uncertainty of the emission cross section of the Cameron system [*Itikawa*, 2002]. Cross sections for direct and dissociative ionization of CO_2 were adopted from the compilation by *Itikawa* [2002]. All cross sections for CO (excitation and ionization) were approximated by semiempirical formulas [*Sawada et al.*, 1972b]. Cross sections for all processes of electron impact on O and N_2 were taken from *Green and Stolarski* [1972], *Jackman et al.* [1977], and the recent compilation by *Itikawa* [2006].

4. Results

[13] To test our model, we first apply it to the conditions of the Viking 1 measurements, that is, a solar zenith angle of 45° and low solar activity. *Fox and Dalgarno* [1979] constructed a model of the Martian atmosphere based upon Viking 1 data and conducted a comprehensive quantitative analysis of the measurements of the ultraviolet dayglow. Comparison of the excitation rates of the two models shows a very good agreement if we use identical atmospheric composition and cross sections. In the following we use the atmosphere extracted from the Mars thermospheric general circulation model of *Bougher et al.* [1990, 1999, 2000, 2004, 2006] for a solar longitude Ls = 180°, a latitude of 47.5°N, and at 1200 LT. The altitude profiles of the main neutral species are shown in Figure 1.

4.1. Steady State Fluxes of Electrons in the Martian Thermosphere

[14] We now illustrate some results on the electron energy spectra obtained with the Monte Carlo code of electron

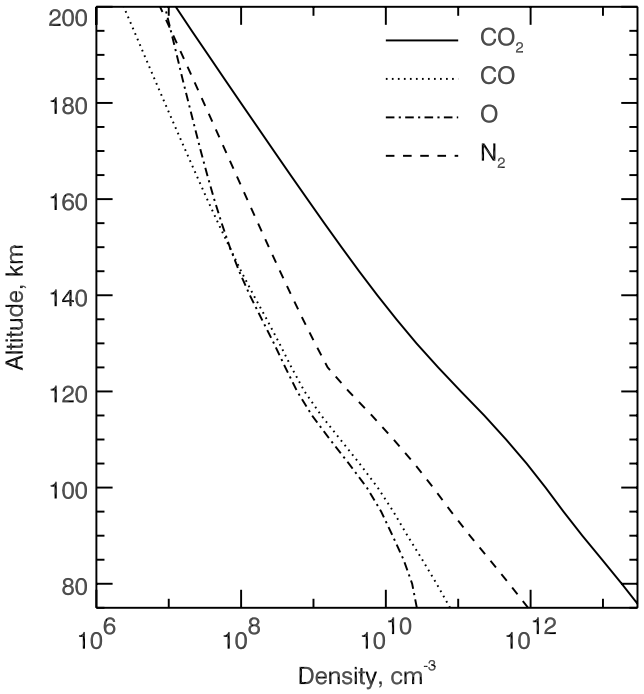

Figure 1. Altitude profile of the main neutral species for the case illustrated in this study.

transport. The calculated energy distribution function for primary (photoelectrons) and secondary electrons at height 135 km is presented in Figure 2 (top). This altitude is selected since it corresponds to the approximate location of the maximum energy deposition of electrons. A prominent dip near 3 eV caused by vibrational excitation of CO_2 is observed. At higher energy the spectrum of primary electrons is highly structured because of the discrete representation of the solar flux, but collisional energy losses smooth the spectrum, while the initial structure still exists. The electron energy distribution in the Martian ionosphere is characterized by signatures from CO_2 [*Mantas and Hanson*, 1979; *Fox and Dalgarno*, 1979]. CO_2 is ionized by solar UV photons of wavelength less than 90.2 nm. The dominant ionization wavelength is associated with the intense solar He 30.4 nm line, which causes ionization of the CO_2 molecule at the Martian exobase, creating a ground state $CO_2^+(X^2\Pi_g)$ ion and generating a 27 eV photoelectron population. Additional photoelectrons are produced with characteristic energies in the 21–24 eV energy range when the carbon dioxide ions are formed in the electronically excited $A^2\Pi_u$ and $B^2\Sigma_u^+$ states. These are major peaks which dominate the photoelectron energy distribution in the range between 20 and 30 eV in the Martian atmosphere (for details, see of Figure 2 (bottom)). These CO_2 ionization features were recently resolved and identified in the high-altitude photoelectron observations by the electron spectrometer from the Analyzer of Space Plasmas and Energetic Atoms flown on the Mars Express spacecraft [*Frahm et al.*, 2006; *Liemohn et al.*, 2006].

[15] The steady state electron fluxes were calculated and are shown at 135 km in Figure 3. It is seen that the upward and downward fluxes at the peak altitude of the electron energy deposition have approximately the same shape, which indicates the dominant role of collisional processes over transport, while in the Martian upper thermosphere the upward flux becomes dominant. All characteristic features and the shape of the calculated upward electron flux are very similar to the ones of observed high-altitude photoelectron flux [see, e.g., *Liemohn et al.*, 2006, Figure 2]. The direct comparison of the calculated and observed energy spectra of photoelectrons is hampered because (1) the observed spectra are shifted in energy because of the unknown spacecraft charging, (2) an uncertainty exists in the solar flux spectrum which is taken from Earth-based empirical model SOLAR2000 v.2.27 scaled to the heliocentric position of Mars, (3) there is a difference in ionospheric location of observations from the range of solar zenith angles, and (4) the SPICAM electron spectrometer measurements were made at altitudes above 1000 km [*Frahm et al.*, 2006; *Liemohn et al.*, 2006].

4.2. Comparison of Model Calculations with SPICAM Limb Observations

[16] Dayglow SPICAM limb observations cover different Martian seasons and a wide range of solar zenith angles and latitudes. The altitudes scanned by the line of sight generally range between 70 and 400 km. At this date, 46 orbits with suitable dayglow observations are available. For reasons of telemetry limitations but also because of the time

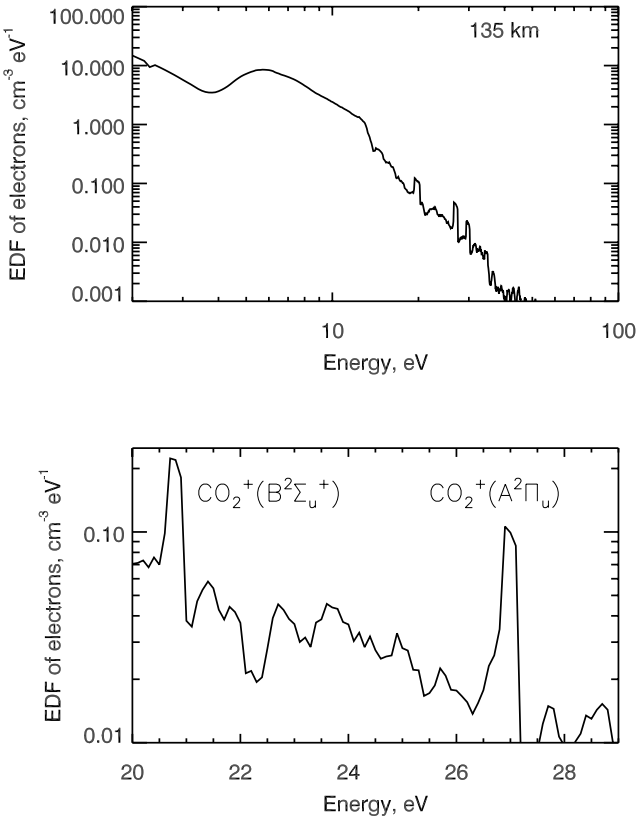

Figure 2. (top) Steady state energy distribution function of electrons and (bottom) expanded view of the CO_2 photoionization peaks calculated at 135 km.

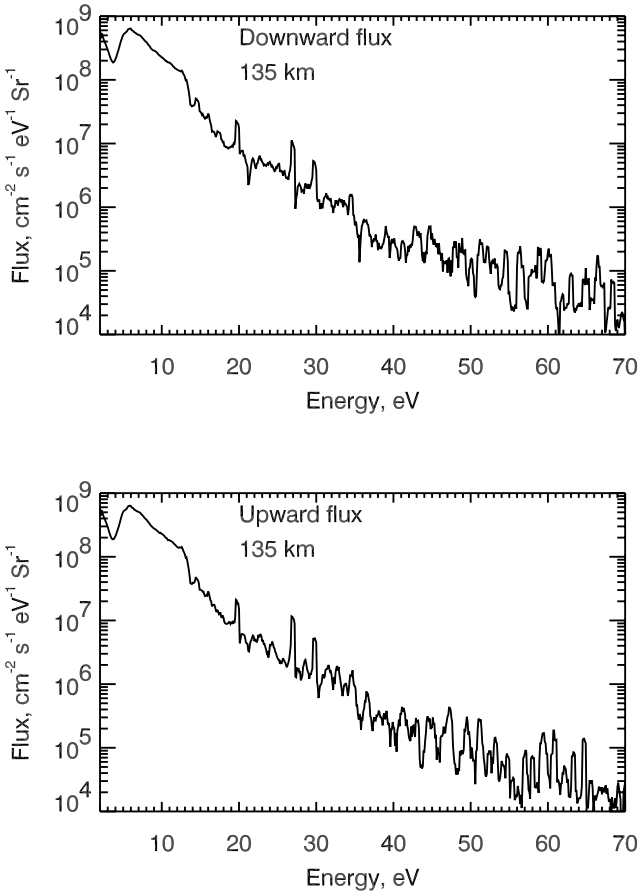

Figure 3. (top) Downward and (bottom) upward electron fluxes at altitude of 135 km.

needed to read all the lines of the charge-coupled device (CCD), only five adjacent parts of the CCD are read out. Each part is called a "spatial bin" and is made of 1, 2, 4, 8, 16, or 32 lines of the CCD following a preselected mode [*Bertaux et al.*, 2006]. Therefore each spatial bin covers a different region of the atmosphere separated by an angular distance ranging from 0.7 to 10.2 arc min, depending on the spatial binning. In the case of orbit 1426 reported here, each spatial bin includes 16 adjacent pixel lines subtending a total angle of 10.2 arc min. All these lines are seen through the small (50 μm) slit, which provides a spectral resolution of 1.5 nm. The SPICAM CCD is read every second, and therefore five spatial bins corresponding to five different and adjacent portions of the SPICAM field of view are recorded each second. In each individual spectrum, nonuniform dark current and offset values are subtracted following the method described by *Leblanc et al.* [2006]. The emission lines are then integrated between selected wavelengths. A typical dayglow observation during a MEX orbit lasts 20 min, centered on the time when MEX is at pericenter near 260 km. During this period a set of 1200 consecutive individual sequences are obtained, each lasting 1 s. Finally, the intensities are calibrated in Rayleighs using well-known hot stars spectra observed by SPICAM during the mission. The accuracy of the absolute intensities is believed to be better than 15% [*Bertaux et al.*, 2006].

[17] For this work we use the airglow observations obtained with SPICAM during MEX orbit 1426 on 26 February 2005. This orbit was arbitrarily selected from typical profiles for quiet solar activity conditions. We have integrated each mean spectrum seen through the small slit between 180 and 270 nm for the CO Cameron system and between 280 and 294 nm for the $CO_2^+(B^2\Sigma^+ - X^2\Pi)$ doublet. At the time of the observations, Ls = 166.5°, the solar activity index $F_{10.7}$ was equal to 76.6 at 1 AU, and the Mars heliocentric distance was equal to 1.50 AU. During the observations discussed below, the solar zenith angle varied between 56.3° at 100 km and 43.3° at 180 km but only changed by 6.8° between 110 and 150 km. A total of 191 spectra were used to generate the SPICAM limb profile between 100 and 180 km.

[18] In Figure 4 we present the calculated altitude profiles of the photoelectron impact sources of atomic oxygen 130.4 and 135.6 nm emissions, the major sources of CO Cameron bands, and CO_2^+ $(B^2\Sigma^+ - X^2\Pi)$ band system for a solar zenith angle (SZA) = 48°. The segment of Mars Express orbit 1426 considered here covers a range of solar zenith angles.

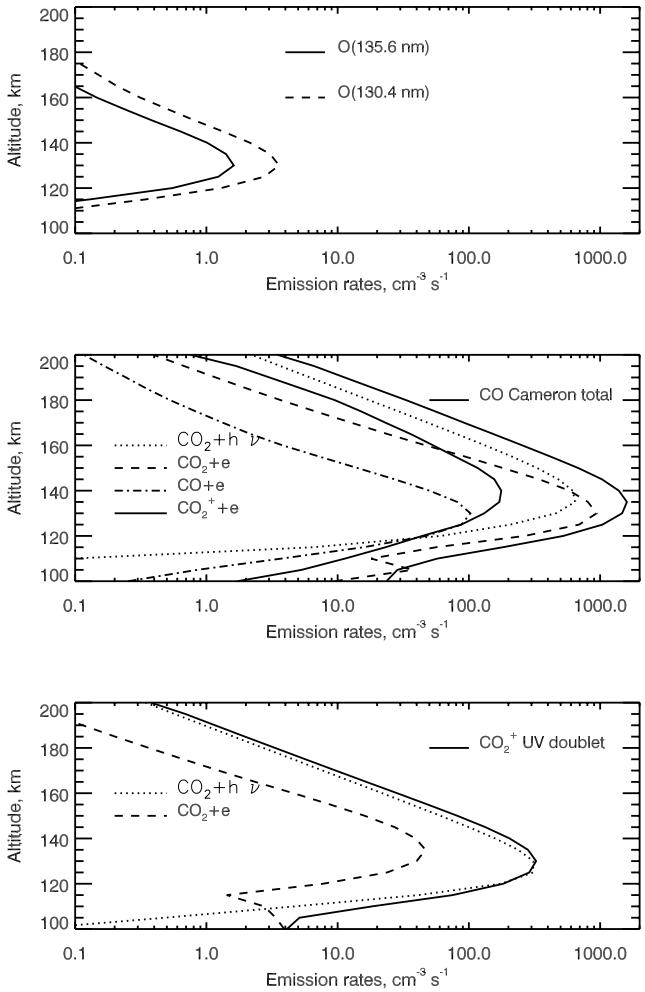

Figure 4. Altitude profiles of the (top) photoelectron impact sources of atomic oxygen 130.4 and 135.6 nm emissions, (middle) major sources of CO Cameron bands, and (bottom) CO_2^+ doublet band system calculated for a solar zenith angle of 48°.

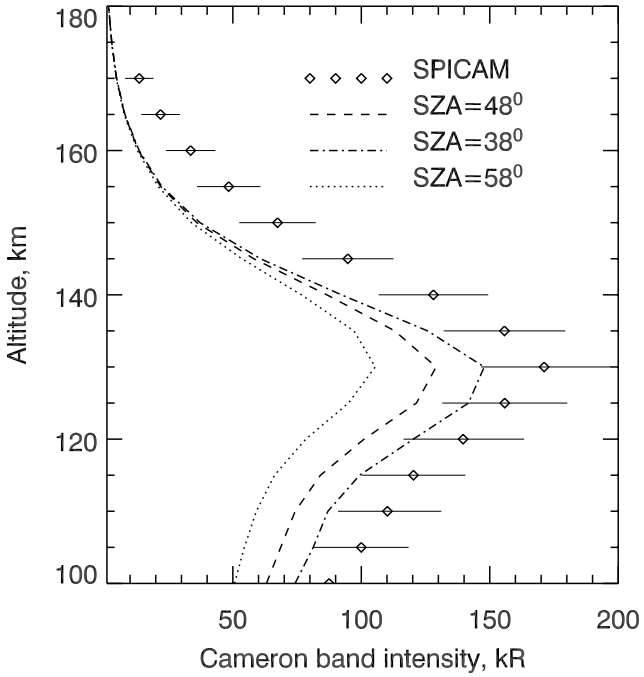

Figure 5. Limb profiles of calculated and observed CO Cameron bands emission rate for MEX orbit 1426. The diamonds show the binned intensities observed by SPICAM, while the lines correspond to the limb brightness calculated with this model for three different solar zenith angles. The variability of the emission rate observed in the five spatial bins and the statistical noise are shown by error bars.

Therefore, to study the effect of the changing solar zenith angle during the altitude scan, we calculate two additional cases with SZA = 38° and 58° using the same neutral atmosphere. CO_2^+ dissociative recombination is not included as a source of CO Cameron bands in the model. To calculate this source, it is necessary to know not only the ion and electron densities but the electron temperature as well. The current model concentrates on electron transport and does not include ion-molecular chemistry. To evaluate the contribution of this source, we use the results from the study by *Fox* [2004] where the densities of CO_2^+ and electrons were calculated for low solar activity. Using these values of densities, the electron temperature adopted by *Hanson et al.* [1977], the rate coefficient of *Seiersen et al.* [2003], and the recent measurements of branching ratios of dissociative recombination of CO_2^+ into the $a^3\Pi$ state (equal to 0.18 according to *Skrzypkowski et al.* [1998] and *Rosati et al.* [2003]), the contribution of the CO_2^+ dissociative recombination can be evaluated. This production rate is shown in Figure 4 (middle). The contribution of this source at the peak altitude is less by factor of about 6 than dissociative excitation by solar UV photons and photoelectrons; nevertheless, we include it in the calculation of the CO Cameron bands intensities.

[19] To compare the results of our model with limb observations, the calculated volume emission rate is integrated along the line of sight, and we select the SPICAM data for orbit 1426 that correspond to the adopted date. The integration is performed in such a way that the brightness for each tangent point altitude is given by

$$I(z_{tg}) = 2\int_0^\infty P(s)e^{-\tau}ds,$$

where s is the distance from the tangent point to a point along the line of sight and $P(s)$ is the corresponding emission rate. In this integral and for the range of altitudes considered here, atmospheric absorption of the Cameron bands and CO_2^+ doublet emission is negligible, and the exponential attenuation factor $e^{-\tau}$ is equal to unity. The factor of 2 comes from the symmetry of the integral with respect to the tangent point.

[20] The calculated and extracted CO Cameron bands emission rates versus altitude are given in Figure 5. The comparison for CO_2^+ ($B^2\Sigma^+ - X^2\Pi$) doublet is displayed in Figure 6. The observed limb profile was averaged over all five bins as was done by *Leblanc et al.* [2006]. In addition, the variability between different spatial bins and the statistical noise of measurements is shown as error bars in Figures 5 and 6. It is seen that the calculated and observed intensities both for CO Cameron bands and for CO_2^+ ($B^2\Sigma^+ - X^2\Pi$) are in a good agreement. The peaks of the Cameron bands are located at the same positions within the vertical resolution of the model (±2.5 km). However, the model predicts a peak altitude for CO_2^+ ($B^2\Sigma^+ - X^2\Pi$) about 5 km below the observed altitude. The difference in peak

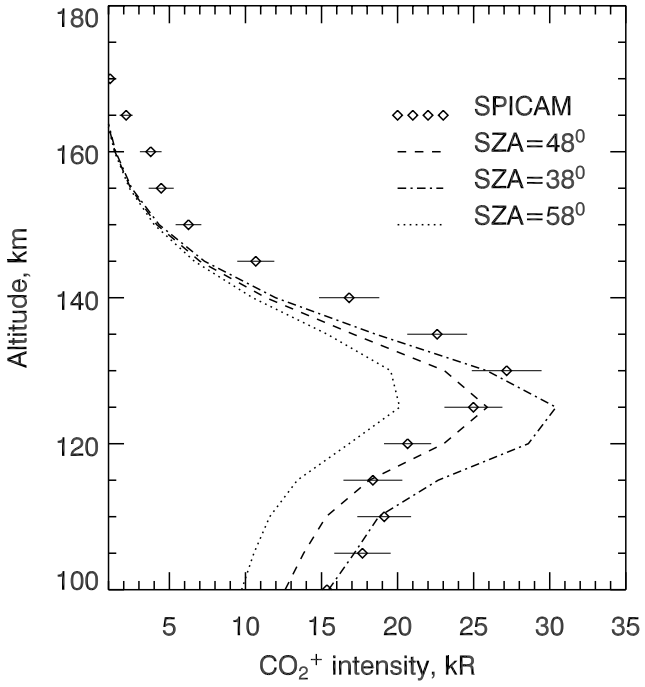

Figure 6. Limb profiles of calculated and observed CO_2^+ ($B^2\Sigma^+ - X^2\Pi$) doublet band system emission rate for orbit 1426. The diamonds show the binned intensities observed by SPICAM, while the lines correspond to the limb brightness calculated with this model for three different solar zenith angles. The variability of the emission rate observed in the five spatial bins and the statistical noise are shown by error bars.

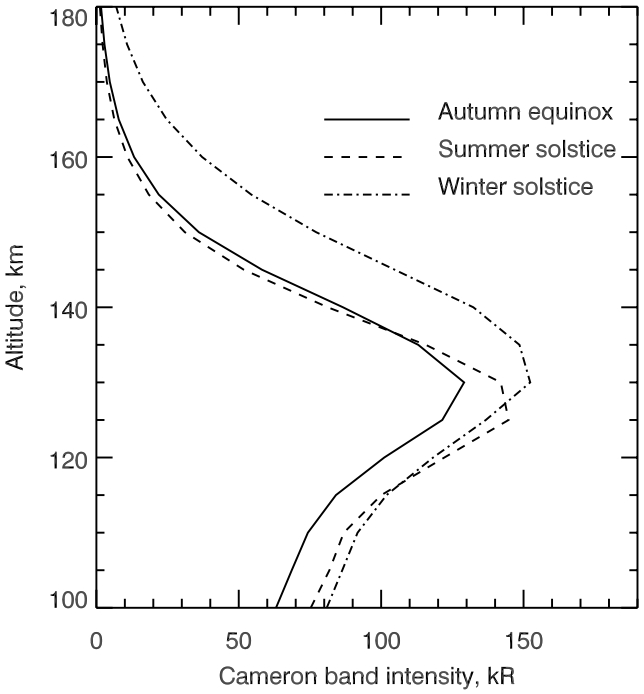

Figure 7. Limb profiles of calculated CO Cameron bands emission rate for three values of the solar longitude (Ls = 73.8°, summer solstice; 166.5°, autumn equinox; and 271.8°, winter solstice) at noontime and solar zenith angle of 48°.

intensity for CO Cameron bands is about 30%. For the CO_2^+ ($B^2\Sigma^+ - X^2\Pi$) doublet the calculated intensities differ from observations by only 10%, which is well within the uncertainties of electron impact cross sections. The differences are thus less than the uncertainties in the input parameters of the model. The difference between the observed and the modeled intensities may be considered as small and quite acceptable considering the (1) uncertainties on the absolute calibration of the spectrograph, (2) statistical noise due to the count rate and background subtraction, (3) differences between the measured (or calculated) excitation cross sections of Cameron and CO_2^+ bands existing in the literature, (4) rather large uncertainties on the neutral atmosphere, and (5) presence of intensity gradients observed with SPICAM which exceed those expected between adjacent regions of the atmosphere.

4.3. Seasonal Variations of the CO Cameron Bands and CO2+ ($B^2\Sigma^+ - X^2\Pi$) Band System Intensities

[21] To evaluate the seasonal variations of the Martian dayglow emissions, we have conducted two additional calculations for 14 August 2004 ($F_{10.7}$ = 138.6 and the Mars heliocentric position at 1.67 AU) and 19 August 2005 ($F_{10.7}$ = 98.5 and the Mars heliocentric position at 1.39 AU). Together with the case of 26 February 2005 ($F_{10.7}$ = 76.6), described in section 4.2, these calculations correspond to three different seasons with Ls = 73.8° (summer solstice), 166.5° (autumn equinox), and 271.8° (winter solstice) in the northern hemisphere. The atmosphere for these dates was again extracted from the Mars thermospheric general circulation model [*Bougher et al.*, 2004, 2006]. All calculations were conducted for noontime and for a solar zenith angle of 48°. The solar fluxes were adopted from the SOLAR2000 research-grade v2.27 EUV solar spectrum model and were scaled as $(1/r_{MS})^2$, where r_{MS} is the heliocentric position of Mars for the dates given above. With such scaling the $F_{10.7}$ indexes of solar activity at Mars orbit are equal to 49.7 for 14 August 2004, 39.1 for 26 February 2005, and 50.0 for 19 August 2005. It is seen that solar activity levels for summer and winter solstices were practically the same. In addition, the time shifting to account for the solar longitude difference between the Earth, Mars, and Sun can be estimated using the technique given by *Mitchell et al.* [2001]. We used the estimates of this effect using the Mars UV proxies from the Web site (http://sprg.ssl.berkeley.edu/~brain/) of the Space Sciences Laboratory of the University of California, Berkeley, and found that both Mars distance and Sun-Earth-Mars phase angle resulted in values of 32.5, 36.6, and 38.0 of solar activity indices at Mars for the dates under study.

[22] The calculated CO Cameron bands and CO_2^+($B^2\Sigma^+ - X^2\Pi$) band system intensities at the limb versus the altitude of the tangent point are given in Figures 7 and 8, respectively. It is seen that the seasonal effect induces intensity variations in the range of 15–20%. These variations are interpreted as a seasonal effect because the solar activity levels are relatively close for the Mars seasons considered in the present study. It is necessary to keep in mind that the procedure described above to scale the solar UV flux at Mars is an approximate one. The most significant feature is the increase of the peak altitudes for both CO Cameron and CO_2^+ ($B^2\Sigma^+ - X^2\Pi$) band systems between northern summer and winter solstice conditions. This

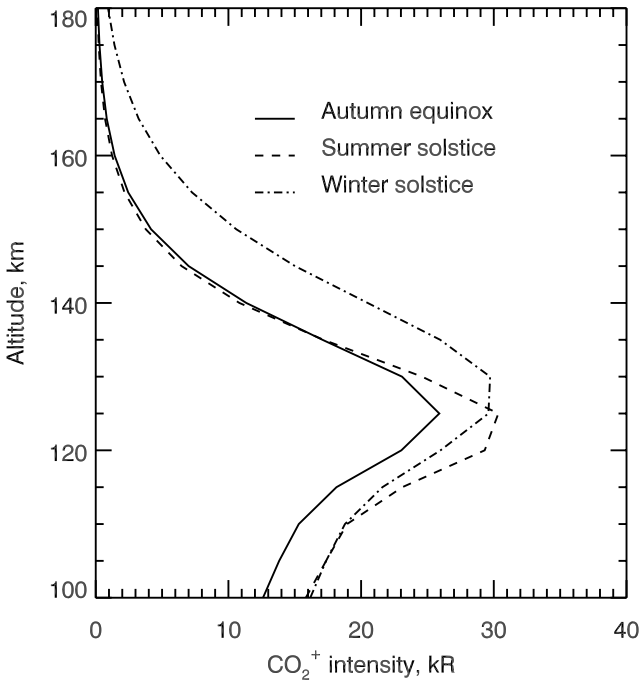

Figure 8. Limb profiles of calculated CO_2^+ ($B^2\Sigma^+ - X^2\Pi$) band system emission rate for three seasons. (Ls = 73.8°, summer solstice; 166.5°, autumn equinox; and 271.8°, winter solstice) at noontime and solar zenith angle of 48°.

change reflects the variation of the atmospheric pressure between the two seasons and the corresponding variation of the altitude of the pressure levels.

5. Conclusions

[23] A Monte Carlo model of the electron transport for the calculations of the collision-induced component of the Mars dayglow emissions has been developed. Additional contributions of direct solar excitation are included, and the model has been compared with SPICAM observations of CO and CO_2^+ FUV emissions. It is found that the model reproduces well the observations with the adopted values of collision and excitation cross sections. The peak altitudes are approximately the same for both CO Cameron bands and the CO_2^+ ($B^2\Sigma^+ - X^2\Pi$) doublet. The differences between those calculated for a mean value of SZA = 48° and observed emission rates for the CO Cameron bands and CO_2^+ ($B^2\Sigma^+ - X^2\Pi$) doublet are less than 30 and 10% in the peak region, respectively. Such comparison appears satisfactory because the uncertainties in the value of the excitation cross section of the CO Cameron bands by electron impact are more than a factor of 2. Calculations suggest the presence of seasonal variations of the altitude of the peak emissions of the CO Cameron bands and CO_2^+ ($B^2\Sigma^+ - X^2\Pi$) bands. This model will be used for further detailed analysis of the Martian and Venusian dayglow observations.

[24] **Acknowledgments.** The authors thank the SPICAM and the Mars Express team for making the data available. J. C. Gérard is supported by the Belgian Fund for Scientific Research (FNRS). This work was also supported by RFBR grant 05-02-17165 and funded by the Belgian National Fund for Collective Fundamental Research (FRFC grant 2.4517.02) and by the PRODEX programme managed by the European Space Agency in collaboration with the Belgian Federal Science Policy Office.

References

Ajello, J. M. (1971), Emission cross sections of CO_2 by electron impact in the interval 1260–4500 Å. II, *J. Chem. Phys.*, *55*, 3169–3177.

Barth, C. A., C. W. Hord, J. B. Pearce, K. K. Kelly, G. P. Anderson, and A. I. Stewart (1971), Mariner 6 and 7 Ultraviolet Spectrometer Experiment: Upper atmosphere data, *J. Geophys. Res.*, *76*, 2213–2227.

Barth, C. A., A. I. Stewart, C. W. Hord, and A. L. Lane (1972), Mariner 9 Ultraviolet Spectrometer Experiment: Mars airglow spectroscopy and variations in Lyman alpha, *Icarus*, *17*, 457–462.

Bertaux, J. L., et al. (2000), The study of the Martian atmosphere from top to bottom with SPICAM light on Mars Express, *Planet. Space Sci.*, *48*, 1303–1320.

Bertaux, J.-L., et al. (2006), SPICAM on Mars Express: Observing modes and overview of UV spectrometer data and scientific results, *J. Geophys. Res.*, *111*, E10S90, doi:10.1029/2006JE002690.

Bisikalo, D. V., V. I. Shematovich, and J.-C. Gérard (1995), A kinetic model of the formation of the hot oxygen geocorona: 2. Influence of O^+ ion precipitation, *J. Geophys. Res.*, *100*, 3715–3720.

Bougher, S. W., R. G. Roble, E. C. Ridley, and R. E. Dickinson (1990), The Mars thermosphere: 2. General circulation with coupled dynamics and composition, *J. Geophys. Res.*, *95*, 14,811–14,827.

Bougher, S. W., S. Engel, R. G. Roble, and B. Foster (1999), Comparative terrestrial planet thermospheres: 2. Solar cycle variation of global structure and winds at equinox, *J. Geophys. Res.*, *104*, 16,591–16,611.

Bougher, S. W., S. Engel, R. G. Roble, and B. Foster (2000), Comparative terrestrial planet thermospheres: 3. Solar cycle variation of global structure and winds at solstices, *J. Geophys. Res.*, *105*, 17,669–17,692.

Bougher, S. W., S. Engel, D. P. Hinson, and J. R. Murphy (2004), MGS Radio Science electron density profiles: Interannual variability and implications for the Martian neutral atmosphere, *J. Geophys. Res.*, *109*, E03010, doi:10.1029/2003JE002154.

Bougher, S. W., J. M. Bell, J. R. Murphy, M. A. Lopez-Valverde, and P. G. Withers (2006), Polar warming in the Mars thermosphere: Seasonal variations owing to changing insolation and dust distributions, *Geophys. Res. Lett.*, *33*, L02203, doi:10.1029/2005GL024059.

Erdman, P. W., and E. C. Zipf (1983), Electron-impact excitation of the Cameron system ($a^3\pi \rightarrow X^1\Sigma$) of CO, *Planet. Space Sci.*, *31*, 317–321.

Feldman, P. D., E. B. Burgh, S. T. Durrance, and A. F. Davidsen (2000), Far-ultraviolet spectroscopy of Venus and Mars at 4 Å resolution with the Hopkins Ultraviolet Telescope on Astro-2, *Astrophys. J.*, *538*, 395–400.

Fox, J. L. (2004), CO_2^+ dissociative recombination: A source of thermal and nonthermal C on Mars, *J. Geophys. Res.*, *109*, A08306, doi:10.1029/2004JA010514.

Fox, J. L., and A. Dalgarno (1979), Ionization, luminosity, and heating of the upper atmosphere of Mars, *J. Geophys. Res.*, *84*, 7315–7333.

Frahm, R. A., et al. (2006), Carbon dioxide photoelectron energy peaks at Mars, *Icarus*, *182*, 371–382.

Furlong, J. M., and W. R. Newell (1996), Total cross section measurement for the metastable $a^3\Pi$ state of CO, *J. Phys. B At. Mol. Opt. Phys.*, *29*, 331–338.

Gérard, J.-C., B. Hubert, D. V. Bisikalo, and V. I. Shematovich (2000), A model of the Lyman-α line profile in the proton aurora, *J. Geophys. Res.*, *105*, 15,795–15,805.

Green, A. E. S., and T. Sawada (1972), Ionization cross sections and secondary electron distributions, *J. Atmos. Terr. Phys.*, *34*, 1719–1728.

Green, A. E. S., and R. S. Stolarski (1972), Analytic models of electron impact excitation cross sections, *J. Atmos. Terr. Phys.*, *34*, 1703–1717.

Hanson, W. B., S. Sanatani, and D. R. Zuccaro (1977), The Martian ionosphere as observed by the Viking retarding potential analyzers, *J. Geophys. Res.*, *82*, 4351–4367.

Huebner, W. F., J. J. Keady, and S. P. Lyon (1992), Solar photo rates for planetary atmospheres and atmospheric pollutants, *Astrophys. Space Sci.*, *195*, 1–289.

Itikawa, Y. (2002), Cross sections for electron collisions with carbon dioxide, *J. Phys. Chem. Ref. Data*, *31*(3), 749–767.

Itikawa, Y. (2006), Cross sections for electron collisions with nitrogen molecules, *J. Phys. Chem. Ref. Data*, *35*(1), 31–53.

Jackman, C. H., R. H. Garvey, and A. E. S. Green (1977), Electron impact on atmospheric gases: 1. Updated cross sections, *J. Geophys. Res.*, *82*, 5081–5090.

Krasnopolsky, V. A., and P. D. Feldman (2002), Far ultraviolet spectrum of Mars, *Icarus*, *160*, 86–94.

Leblanc, F., J. Y. Chaufray, J. Lilensten, O. Witasse, and J.-L. Bertaux (2006), Martian dayglow as seen by the SPICAM UV spectrograph on Mars Express, *J. Geophys. Res.*, *111*, E09S11, doi:10.1029/2005JE002664.

Liemohn, M. W., et al. (2006), Numerical interpretation of high-altitude photoelectron observations, *Icarus*, *182*, 383–395.

Mantas, G. P., and W. B. Hanson (1979), Photoelectron fluxes in the Martian ionosphere, *J. Geophys. Res.*, *84*, 369–385.

Mitchell, D. L., R. P. Lin, C. Mazelle, H. Rème, P. A. Cloutier, J. E. P. Connerney, M. H. Acuña, and N. F. Ness (2001), Probing Mars' crustal magnetic field and ionosphere with the MGS Electron Reflectometer, *J. Geophys. Res.*, *106*, 23,419–23,427.

Opal, C. B., W. K. Peterson, and E. C. Beaty (1971), Measurements of secondary-electron spectra produced by electron impact ionization of a number of simple gases, *J. Chem. Phys.*, *55*, 4100–4106.

Porter, H. S., and F. W. Jump (1978), Analytic total and angular elastic electron impact cross sections for planetary atmospheres, *Rep. CSC/TM-6017*, Goddard Space Flight Cent., Greenbelt, Md.

Porter, H. S., F. Varosi, and H. G. Mayr (1987), Iterative solution of the multistream electron transport equation: 1. Comparison with laboratory beam injection experiments, *J. Geophys. Res.*, *92*, 5933–5959.

Rosati, R. E., R. Johnsen, and M. F. Golde (2003), Absolute yields of CO ($a'\,^3\Sigma^+$, $d\,^3\Delta_i$, $e\,^3\Sigma^-$) + O from the dissociative recombination of CO_2^+ ions with electrons, *J. Chem. Phys.*, *119*, 11,630–11,635.

Sawada, T., D. J. Strickland, and A. E. S. Green (1972a), Electron energy deposition in CO_2, *J. Geophys. Res.*, *77*, 4812–4818.

Sawada, T., D. L. Sellin, and A. E. S. Green (1972b), Electron impact excitation cross sections and energy degradation in CO, *J. Geophys. Res.*, *77*, 4819–4828.

Seiersen, K., A. Al-Khalili, O. Heber, M. J. Jensen, I. B. Nielsen, H. B. Pedersen, C. P. Safvan, and L. H. Andersen (2003), Dissociative recombination of the cation and dication of CO_2, *Phys. Rev. A*, *68*(2), 022708, doi:10.1103/PhysRevA.68.022708.

Shematovich, V. I., D. V. Bisikalo, and J.-C. Gérard (1994), A kinetic model of the formation of the hot oxygen geocorona: 1. Quiet geomagnetic conditions, *J. Geophys. Res.*, *99*, 23,217–23,228.

Skrzypkowski, M. P., T. Gougousi, R. Johnsen, and M. F. Golde (1998), Measurement of the absolute yield of CO ($a^3\pi$) + O products in the dissociative recombination of CO_2^+ ions with electrons, *J. Chem. Phys.*, *108*, 8400–8407.

Solomon, S. C. (2001), Auroral particle transport using Monte Carlo and hybrid methods, *J. Geophys. Res.*, *106*, 107–116.

Stewart, A. I., C. A. Barth, C. W. Hord, and A. L. Lane (1972), Mariner 9 Ultraviolet Spectrometer Experiment: Structure of Mars' upper atmosphere, *Icarus*, *17*, 469–474.

Tobiska, W. K. (2004), SOLAR2000 irradiances for climate change, aeronomy and space system engineering, *Adv. Space. Res.*, *34*, 1736–1746.

D. V. Bisikalo and V. I. Shematovich, Stellar Physics and Evolution, Institute of Astronomy, Russian Academy of Sciences, 48 Pyatnitskaya Street, Moscow 119017, Russia. (shematov@inasan.rssi.ru)

S. W. Bougher, Atmospheric, Oceanic and Space Sciences, College of Engineering, University of Michigan, Ann Arbor, MI 48109, USA.

C. Cox and J.-C. Gérard, Laboratoire de Physique Atmosphérique et Planétaire, Université de Liège, B-4000 Liège, Belgium.

F. Leblanc, Service d'Aeronomie du CNRS, Verrieres le Buisson, F-91371, France.